

STRUCTURAL AND DIELECTRIC PROGRESSION OF 5 % Gd DOPED BiFeO₃ NANOPARTICLES THROUGH Cr (2-8%) DOPING

M. N. Hossain^{*1}, M. A. Matin¹, M. M. Rhaman^{1,2}, M. A. Ali³, M. A. Hakim¹, S. K. Roy^{*3}

¹ Department of Glass and Ceramic Engineering (GCE), Bangladesh University of Engineering and Technology (BUET), Dhaka 1000, Bangladesh.

² Department of Electrical and electroni Engineering, Ahsanullah University of Science and Technology, Dhaka, Bangladesh.

³ Department of Physics, Chittagong University of Engineering and Technolgy (CUET), Chattogram 4349, Bangladesh;

Received: 28 October, 2021

Accepted: 26 December, 2021

ABSTRACT

This study reports the structural modifications in undoped multiferroic BiFeO₃ (bismuth ferrite or BFO) nanoparticles caused by doping at both the A-site (by 5% Gd) and B-site (by 2-8% Cr) and the resulting improvements in dielectric characteristics. Both un-doped and doped BFO nanoparticles were synthesized using the sol-gel technique and annealed at 600°C for crystallization. X-ray diffractometry (XRD) reveals a phase transition from rhombic (R_{3c}) to orthorhombic (P_{n21d}). Field Emission Scanning Electron Microscopy (FESEM) study shows the production of nanoparticles with sizes ranging from 80 to 130 nm. Impedance analyzer experiments (100 Hz-10 MHz) show that the dielectric characteristics of doubly doped BFO are very stable over a wide frequency range. The dielectric permittivity of co-doped BFO decreases with Cr doping concentration up to $x = 0.06$ before reversing. The conductivity drops dramatically as the Cr content rises.

Keywords: Nanoparticles, BiFeO₃, Microstructure, Dielectrics, Electron microscopy, AC conductivity

1. INTRODUCTION

Multiferroic materials feature two or more forms of ordering in a single phase, such as ferromagnetic and ferroelectricity (Catalan and Scott, 2009; Wu, 2016). By applying an electric, magnetic, or stress field to a multiferroic material, any ferroic attribute can be altered, making them interesting for both fundamental study and practical applications. The coexistence of several order parameters in multiferroics reveals unexpected physical phenomena and opens the door to new device functions like as magneto-electric, magneto-optic, and other novel coupling features like spintronics, memory device, nonvolatile logic, etc. (Allibe, 2012; Catalan, 2009; Eerenstein, 2006; Kumar, 2014; Khomskii, 2009; Sosnowskat, 1982; Wu, 2016; Zheng, 2018). BFO is recognized to be one of several studied multiferroics that exhibit ferro-electromagnetism at ambient temperature, which bodes well for the design and development of technological devices with innovative functions. BFO shows a strong dielectric permittivity and high magnetic permeability, and, therefore, it could replace the inductor and capacitor in resonant circuit with a single component, allowing portable cellular technology to be miniaturized further (Baettig, 2005; Qi, 2012). On the other hand, the multi-domain nature of the material tends to cancel out the features of interest, making a thorough understanding of the structural evolution responsible for such properties more challenging. For example, BFO, the material of interest, has several drawbacks associated with electrical properties, such as, a high leakage current along with weak magnetization and small ferroelectric spontaneous polarization limits its potential applications (Qi, 2012). Materials must be designed suitably to attain desired properties in order to eliminate these drawbacks. Doping is a purposeful insertion of impurities into a lattice in order to improve the material's characteristics. Doping in both the A and B sites of perovskite structured materials (Chaudhuri, 2012; Matin, 2019; Matin M.A, 2019; Rahman, 2019) has been proven to be a promising approach to improve multiferroic characteristics. To fulfill the needs of today's nanotechnology era, a proper doping concentration must be figured out to modify structure-property interactions, which is crucial in the development of new materials. This study aims to investigate evolution of dielectric properties of undoped BFO by simultaneous doping of 5% Gd at A-site and 2-8% doping of Cr at B site.

BFO multiferroics belongs to ABO₃ family. In the deformed perovskite lattice, BFO invariably crystallizes with the rhombohedral structure (space group, R_{3c}), with Bi³⁺ ions occupying the A-site and Fe³⁺ ions occupying the B-site (Kuo, 2016; Mukherjee, 2014). The super-exchange interaction between Fe^{3p} and O^{2p} ions has been shown

*Corresponding Author: nazmul.hossain.gce.buet@gmail.com; skroy@cuet.ac.bd

<https://www2.kuet.ac.bd/JES/>

ISSN 2075-4914 (print); ISSN 2706-6835 (online)

to play a vital role in the ferromagnetic characteristics of BFO. The off-center displacement of $6s^2$ lone pair electrons in Bi^{3+} ions cause ferroelectric characteristics (Khomchenko, 2017; Si, 2018). However, because the impurity phases (such as $\text{Bi}_2\text{Fe}_4\text{O}_9$, $\text{Bi}_{24}\text{FeO}_{40}$, and others) are mixed in BFO's rhombohedral phase, it always has a long-range spin cycloid structure (Kuo, 2016), which restricts its practical applications (Dutta, 2018; Yu, 2016). As a result, significant efforts have been made to improve the structures and properties of BFO through ions doping, such as A-site doping rare-earth (Er^{3+} , La^{3+} , Sm^{3+} , and Ho^{3+} , Gd^{3+} , etc.) or divalent alkaline-earth metal ions (Ba^{2+} , Ca^{2+} , Sr^{2+} , etc.), and B-site doping transition metal ions (Cr^{3+} , Mn^{4+} , Ti^{4+} , etc.) (Chaudhuri, 2012; Dutta, 2018; Khomchenko, 2017; Kumar, 2014; Kuo, 2016; Matin, 2019; Matin *et al.*, 2019; Mukherjee, 2014; Qi, 2012; Rhaman, 2019; Si, 2018; Yu, 2016). Doping with a new magnetic ion, such as lanthanide, is an effective way to suppress phase impurities and improve the remanent magnetization of BFO systems. Because of its large magnetic moment of $7.94 \mu_B$, doping with Gd^{3+} as of lanthanide elements in the A site, can be used to improve the magnetic properties of BFO (Matin *et al.*, 2019). Furthermore, the ionic radius mismatch between Gd^{3+} and Bi^{3+} induces lattice distortion, which has a significant impact on BFO's magnetic and electric properties. Transition metal ions, such as isovalent Cr^{3+} on the B-site, on the other hand, can preserve charge neutrality and restrict oxygen vacancies to a minimum. During doping, Fe^{3+} and Cr^{3+} occupy the B site randomly, causing the cation gap between oxygen octahedral to be distorted. According to Kanamori rule (Dong, 2015; Wohlfeld, 2011; Yoo, 2015), the spin coupling of the $\text{Fe } d^5 - \text{O} - \text{Cr } d^3$ link is expected to establish ferromagnetic ordering in the perovskite, whereas the stereo-active $6s^2$ lone pair is thought to give birth to ferroelectricity. As a result of the transition group dopant infiltration, BFO's magnetic and ferroelectric properties are expected to improve. 15% Gd doping in place of Bi has been reported to improve dielectric characteristics of BFO (Matin M. A., 2019). The partial substitution of Fe by Cr at B site has found to reduce dielectric loss (Matin M. A., 2019, Kumar, 2011). However, simultaneous doping of Gd^{3+} (5 wt% of Gd) at A-site and varying Cr^{3+} ion concentration at B-site and studying their effects on dielectric properties are not reported yet. As a result, we used the sol-gel method to make Gd and Cr doped BFO multiferroic nanoparticles, with the goal of determining how simultaneous doping of 5% Gd in the A site and 2-8% Cr in the B site affects the structure of doped BFO and the associated dielectric properties when compared to undoped BFO.

2. EXPERIMENTAL

The sol-gel process was used to make un-doped and doped BFO nanoparticles. The precursor materials $\text{Fe}(\text{NO}_3)_3 \cdot 9\text{H}_2\text{O}$ (Mark, India), $\text{Bi}(\text{NO}_3)_3 \cdot 5\text{H}_2\text{O}$ (Mark, India), $\text{Gd}(\text{NO}_3)_3 \cdot 6\text{H}_2\text{O}$, and $\text{Cr}(\text{NO}_3)_2 \cdot 9\text{H}_2\text{O}$ (Sigma-Aldrich Co., Germany) were dissolved in deionized water. As a chelating agent, citric acid ($\text{C}_6\text{H}_8\text{O}_7$) was utilized. The resultant solution was then heated for 5 hours at 85°C . As BFO solution is very acidic ($\text{pH} < 1$), the pH of the solution was maintained at 1.5 by adding base called ammonium hydroxide (NH_4OH) to it drop by drop. Then, as a polymerization agent, ethylene glycol ($\text{C}_2\text{H}_6\text{O}_2$) was utilized. A dense gel was generated after continuous heating and stirring, and it was dried at 110°C for 12 hours in an electric oven to obtain xerogel powder. This powder was then crystallized by annealing it for two hours at 600°C in a high-temperature furnace. The heating/cooling rate was set to $3^\circ\text{C}/\text{min}$. The mix powder sample was then pulverized thoroughly in an agate and mortar as using conventional ceramic technique.

X-Ray Diffractometer (XRD) was used to examine the nanostructure formation and properties of the nanoparticles that had been produced (PANalytical Empyrean, Netherlands). Detail structural factors such as crystallite size and strain were determined via Rietveld refinement (High score plus software) was presented in matching experimental and theoretical data. Field emission scanning electron microscopy (FESEM) was used to see the particle size and surface morphology and semi-quantitative elemental testing of nanostructures (JEOL JSM-7600F). An impedance analyzer was used to test the dielectric characteristics of the samples (Wayne Kerr Electronics Ltd., UK).

Pellet samples were utilized to assess dielectric characteristics. A uniaxial hydraulic pressing machine (HERZOG, Germany) with a 20 kN applied force was used to make the pellets with a thickness of 0.4 mm and a diameter of 5 mm. The pellets were sintered at 600°C for 2 hours. The pellets' thickness and area were measured. After that, silver paste was evenly coated to both sides of each pellet. On each side of the pellet, a copper wire was also connected. The pellets were then dried in an electric oven at 110°C for 12 hours to remove any moisture.

3. RESULTS AND DISCUSSION

3.1 Structure of nanoparticles

XRD experiments were carried out at ambient temperature within a 2θ range of $20\text{-}70^\circ$ to reveal the structural evolution with Cr doping. Figure 2 shows XRD patterns of pure BFO and co-doped $\text{Bi}_{0.95}\text{Gd}_{0.05}\text{Fe}_{1-x}\text{Cr}_x\text{O}_3$ ($x = 0, 0.02, 0.04, 0.06, \text{ and } 0.08$) nanoparticles. All of the synthesized samples show a well-defined crystallinity. The crystallographic planes of diffraction peaks were detected and marked in Figure 1(a). Although a trace secondary

phase was detected, the XRD spectra of un-doped BFO closely match the standard file's rhombohedral phase that belong to R_{3c} space group crystal structure. With 5% Gd doping, there were no secondary phase peaks visible on the XRD pattern. It is worth mentioning that B-site doping by Cr also inhibits such secondary phase forming, because more reactive Cr reacts so quickly in BFO solution that, it does not get chance to form secondary phase. Thus, absence of such secondary phase results in a significant improvement in dielectric characteristics by Cr doping. To calculate the average crystal size (d) of the nanoparticles, we used the Scherrer formula. The formula is given below:

$$d = k\lambda/\beta \cdot \cos\theta,$$

where k =shape factor, which typically has a value of 0.9,

λ =wavelength (1.5418Å) of Cu- K_{α} radiation,

β =full width at half maximum (FWHM) of the highest intensity (110) diffraction peak,

θ =Bragg angle of the diffraction peak.

The calculated grain sizes for all samples are listed in Table 1.

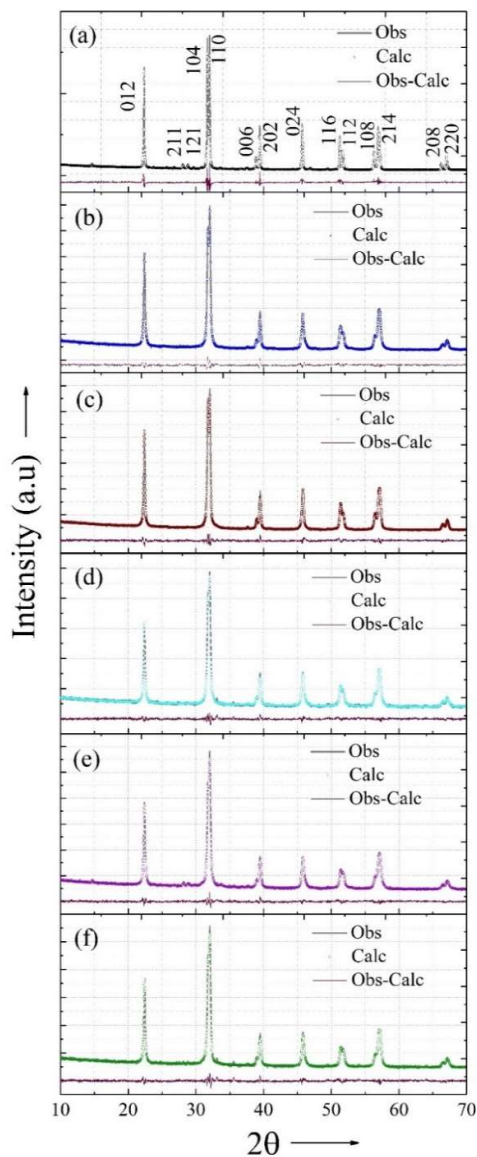


Figure 1: X-ray diffraction patterns of $Bi_{0.95}Gd_{0.05}Fe_{1-x}Cr_xO_3$: (a) $BiFeO_3$, (b) $x = 0$, (c) $x = 0.02$, (d) $x = 0.04$, (e) $x = 0.06$, (f) $x = 0.08$ nanoparticles. BFO phases are indexed as (012), (104), (110), (006), (202), (024), (116), (112), (108), (202), and (208) peaks. Other planes represent secondary phases for $Bi_2Fe_4O_9$ and $Bi_{25}FeO_{39}$.

Additional structural information such as phase, tolerance factor, strain, lattice parameters, and so on was obtained using the Rietveld refinements technique. The goodness of fit (GOF) was found to be fairly good. An un-doped BFO sample's XRD pattern revealed a unique rhombohedral phase with space group R_{3C} . With increasing Cr doping concentrations, the extent of the P_{n21a} phase increased, indicating a phase transition from rhombohedral phase R_{3C} to orthorhombic phase P_{n21a} crystal structure as shown in Table 1. Such a phase shift, which is the purpose of doping, can impact the multiferroic properties of $Bi_{0.95}Gd_{0.05}Fe_{1-x}Cr_xO_3$ ($x = 0, 0.02, 0.04, 0.06$, and 0.08). However, some secondary phases were detected in undoped BFO, which are $Bi_2Fe_4O_9$ and $Bi_{25}FeO_{39}$ respectively and their corresponding planes are indicated in the XRD pattern of Fig. 1 (a). Because of the presence of smaller ionic radii in both the A and B sites of BFO, octahedral rotation of BO_6 (Rhaman, 2019; Matin *et al.*, 2019) can cause the rhombohedral phase to be transformed into another space group rather than R_{3C} . The fundamental process of such phase changes can be explained using a tolerance factor (t) calculation, and the governing equation is stated as, $t = (R_A + R_O) / \sqrt{2}(R_B + R_O)$, where, R_A , R_B , and R_O are radii of the A-site ions, B-site ions, and oxygen ions in $BiFeO_3$, respectively.

Table 1: Rietveld factors, Refined structural parameters, crystallite sizes (d) and lattice strain of $Bi_{0.95}Gd_{0.05}Fe_{1-x}Cr_xO_3$ nanoparticles.

Sample		BFO	x=0.00	x=0.02	x=0.04	x=0.06	x=0.08
Phase(s) present	R_{3C}	100 %	92.1 %	90 %	88.9 %	87.9 %	85.3 %
Unit cell parameters	$a=b$ [Å]	5.57761	5.57214	5.57365	5.57276	5.57458	5.57109
	c [Å]	13.86779	13.83344	13.8317	13.83048	13.84101	13.82681
	V [Å ³]	373.624	371.9677	372.123	371.97	372.4969	371.6487
Average bond lengths	Fe-O [Å]	2.034 Å	2.17306	2.19729	2.07851	2.17494	2.16952
Average bond angles	Fe-O-Fe [°]	146.5661	153.0827	153.1226	153.1303	153.1233	153.1226
Phase(s) present	P_{n21a}	-	7.9 %	10 %	11.1 %	12.1 %	14.7 %
Unit cell parameters	a [Å]	-	5.68834	5.74408	5.74408	5.60034	5.60098
	b [Å]	-	5.5469	5.52682	5.52682	5.5255	5.50197
	c [Å]	-	7.97403	7.8018	7.8018	7.85377	7.84351
	V [Å ³]	-	247.5194	247.6798	247.6798	243.032	241.7089
Particle size, D (nm)		68	28	33	26	25	27
Strain, ϵ		0.186	0.444	0.384	0.488	0.502	0.471
Rietveld factors	R_p	4.65	3.50	3.40	3.51	3.64572	3.44894
	R_{exp}	4.26	4.04	3.38	4.11	4.05	3.79
	R_{wp}	6.29	4.41	4.40	4.50	4.69	4.43
	GOF	1.48	1.09	1.16	1.09	1.16	1.17

When compared to undoped BFO, an A-site substitution of 5% isovalent Gd^{3+} with an ionic radius of 0.938 Å in place of bigger Bi^{3+} (1.03 Å), the tolerance factor in $Bi_{0.95}Gd_{0.05}FeO_3$ drops from 0.8389 to 0.8373. Further B-site substitution of 2–8% Cr^{3+} (0.615 Å) in place of Fe^{3+} (0.645 Å) changes the tolerance factor in $Bi_{0.95}Gd_{0.05}Fe_{1-x}Cr_xO_3$ ($x = 0, 0.02, 0.04, 0.06$, and 0.08) from 0.8376 to 0.8383. Thus, as Cr concentrations rise, tolerance factor (t) rises as well, resulting in decreasing octahedral tilting which causes phase shift from rhombohedral (R_{3C}) to orthorhombic (P_{n21a}), similar to previously documented rare earth (La, Pr, Nd, Sm, Gd) doping in A site (Jonscher, 1977). With 5% Gd doping, the calculated lattice strain increased, and it began to grow more with 2% Cr doping, but it did not follow the sequence. Table 1 shows that the maximum strain of 0.502 was achieved for the 6% Cr doped sample due to lattice distortion. Due to doping, bond length and bond angle have increased, but crystallite size has decreased. Basically, not only the lattice parameters, but also their associated angles, change with structural change (Rhombohedral structure ($a = b$) to Orthorhombic structure ($a \neq b \neq c$)). As a result, if one bond length increases, other bond lengths may decrease, resulting in the observed reduction in volume due to their altered crystal structures.

3.2 Morphology of nanoparticles

Figure 2 shows scanning electron micrographs of pure-BFO and co-doped $\text{Bi}_{0.95}\text{Gd}_{0.05}\text{Fe}_{1-x}\text{Cr}_x\text{O}_3$ nanoparticles. Because of the high surface energy in these nanostructures, particles agglomerate (Jonscher, 1977), and are visible in co-doped BFO nanoparticles. Agglomeration of particles happens when ultra-fine multiferroic nanocrystals form a neck via solid state diffusion at annealing temperatures exceeding 300°C . The shape of the particles in doped BFO is observed to be more uniform than the un-doped equivalent. The particle agglomeration effect is also visible in co-doped BFO nanoparticles. Each micrograph in Figure 2 has the particle size distribution placed on it.

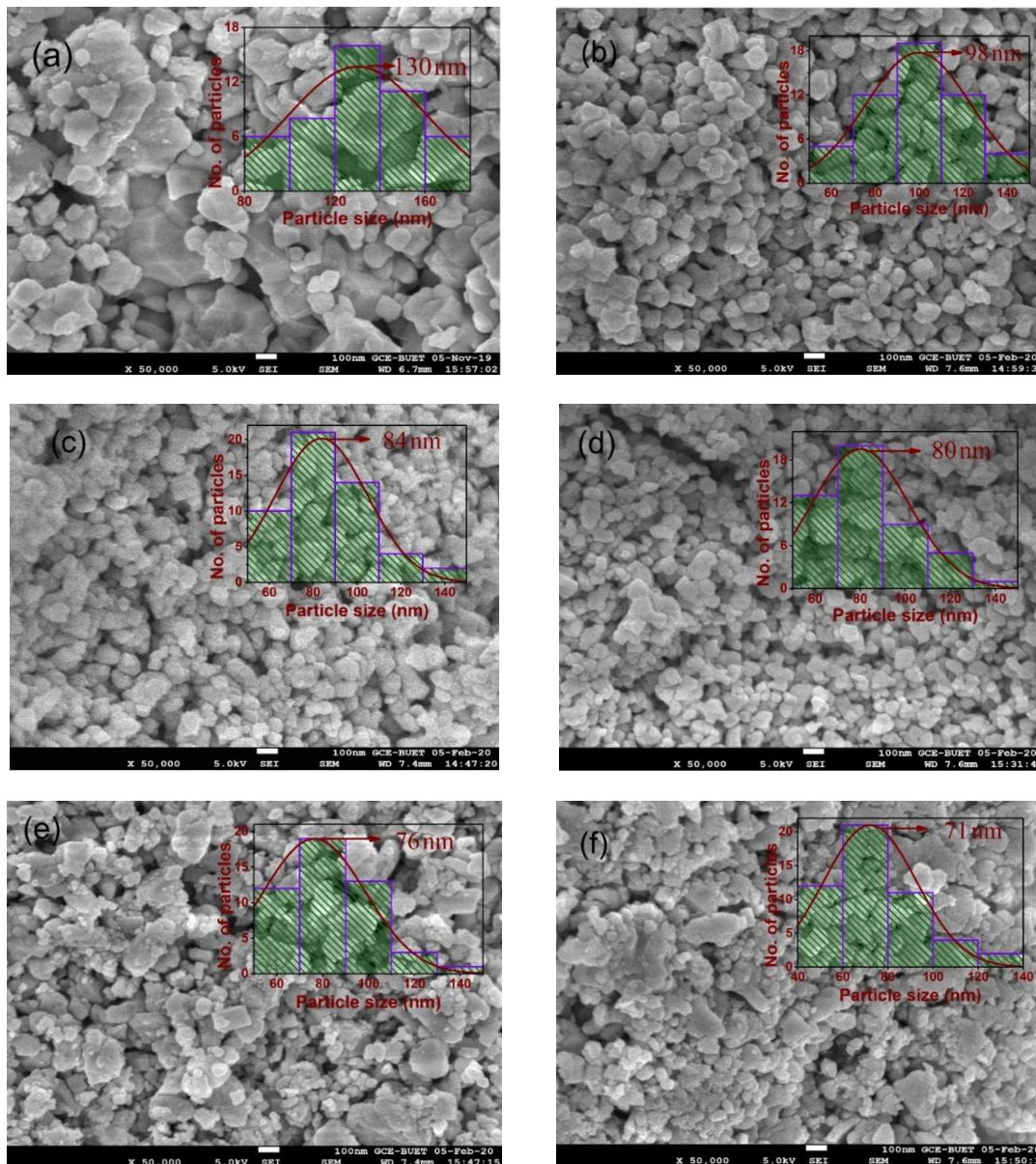


Figure 2: FSEM image of $\text{Bi}_{0.95}\text{Gd}_{0.05}\text{Fe}_{1-x}\text{Cr}_x\text{O}_3$ nanoparticles: a) BiFeO_3 , b) $x = 0$, c) $x = 0.02$, d) $x = 0.04$, e) $x = 0.06$, f) $x = 0.08$.

The average particle size is estimated using ImageJ software, and it is found that with 8% Cr doping, the average particle size is reduced to 71 nm when compared to the un-doped counterpart. Nonetheless, when doping concentrations increase, the crystallite size of co-doped nanoparticles decreases, suggesting a grain growth inhibitory effect caused by Gd and Cr dopants. The discrepancies in ionic radii between the A-site Bi^{3+} (1.03 Å) and Gd^{3+} (0.938 Å) ions and the B-site Fe^{3+} (0.645 Å) and Cr^{3+} (0.615 Å) ions may cause unit cell contraction,

preventing crystallite nucleation, a continuous effect of dispersion and mechanical deformation, and reducing the size of particles in nanoscale.

3.3 Dielectric properties

Dielectric permittivity (ϵ'), dielectric loss factor ($\tan \delta$), AC conductivity (σ_{AC}), resistance (Z'), reactance (Z''), complex impedance spectra, and electrical modulus spectra were used to evaluate the dielectric characteristics of un-doped and doped BFO. In the impedance measurements, parallel-plate capacitors with a frequency range of 100 Hz to 10 MHz were used.

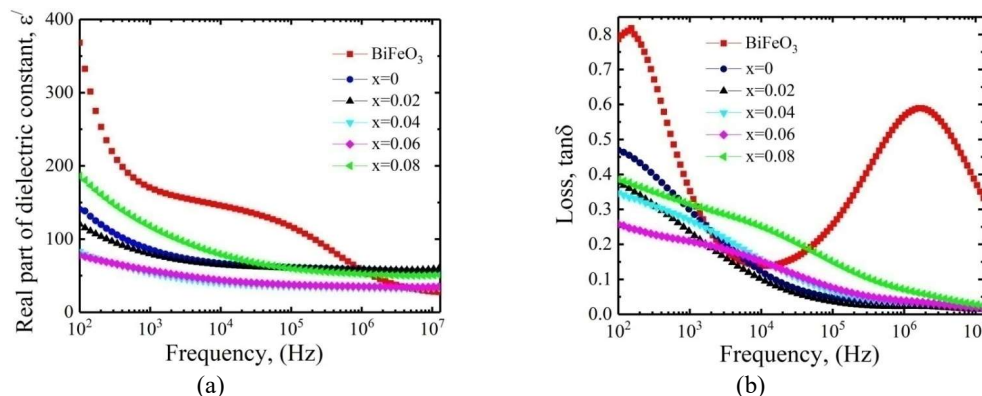


Figure 3: a) Dielectric permittivity (ϵ') and b) Dielectric loss ($\tan \delta$) as a function of frequency for $\text{Bi}_{0.95}\text{Gd}_{0.05}\text{Fe}_{1-x}\text{Cr}_x\text{O}_3$

The changes in dielectric permittivity as a function of frequency are shown in Figure 3 (a) what is very important for multiferroic composites. Dielectric permittivity is estimated to be in the range of 50 to 300 based on sample morphology, orientation, and frequency range, and add to the measured permittivity due to dominating space-charge contribution and domain-wall motion at these frequencies. Doped samples have lower dielectric permittivity values than their un-doped counterparts up to 1 MHz; comparable results have been obtained elsewhere (Bielecki, 2012; Chauhan, 2015; Mao, 2012; Wang, 2013). The dielectric permittivity of co-doped samples, on the other hand, was shown to decrease with Cr doping concentration up to $x = 0.06$ before reversing. The barrier of charge movement and grain size reduction of doped materials may be responsible for such decreasing behaviors up to $x = 0.06$ and similar to reports for Ba-doped (Chauhan, 2013), La-doped (Chaudhuri, 2012), and Sm^{3+} Co-doped BFO samples (Yoo, 2015).

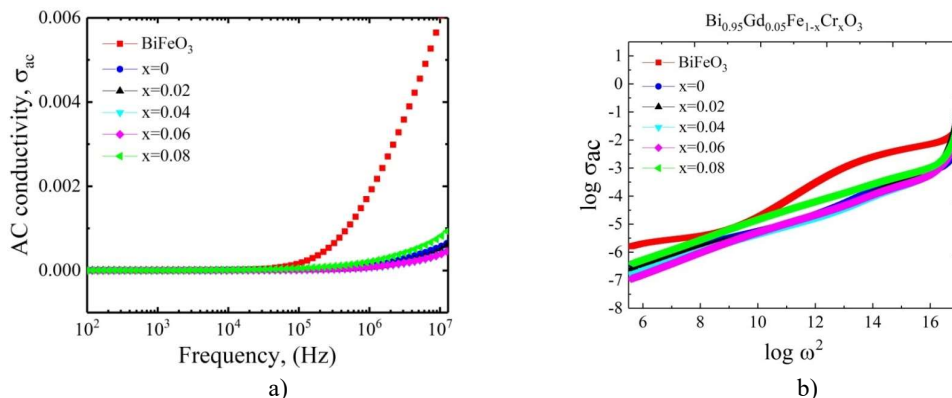


Figure 4: (a) AC conductivity (σ_{AC}) and (b) Plots of $\log(\sigma_{AC})$ vs $\log(\omega^2)$ for $(\text{Bi}_{0.95}\text{Gd}_{0.05}\text{Fe}_{1-x}\text{Cr}_x\text{O}_3)$ sintered at 600°C .

At a low frequency, the real component of dielectric permittivity (ϵ') was found to be at its greatest. It was found to decrease with frequency. When the frequency is low, the decrement is rapid, but as the frequency increases, the rate of decrement slows for a constant value at high frequency, typical to multiferroic materials (Chaudhuri, 2012; Chauhan, 2013). All types of polarization contributed to the first low frequency region but only dipolar and interfacial polarization contributed to a low frequency. In the mid-frequency range, where orientation polarization is mostly responsible for dielectric permittivity, a slower reduction in ϵ' and ϵ'' (imaginary part of dielectric permittivity) is observed. The atomic and electronic polarization is linked to the continuous dielectric characteristics in the high-frequency region (Rhaman, 2020). The most striking result is that pure BFO displays

strong dielectric dispersion which is significantly reduced in doped BFO. Similarly, the dielectric loss was also shown to decrease in doped samples compared to un-doped counterpart indicating a reduction in defect centers (Matin, 2019). Figure 4 (a) shows the variation of AC conductivity (σ_{AC}) as a function of frequency. It reveals that σ_{AC} is invariable up to ≤ 100 kHz and then it increases for all samples. However, a significant decrease of σ_{AC} owing to Gd-Cr co-doping was observed. The decrease of σ_{AC} is due to the same reason as that of dielectric permittivity.

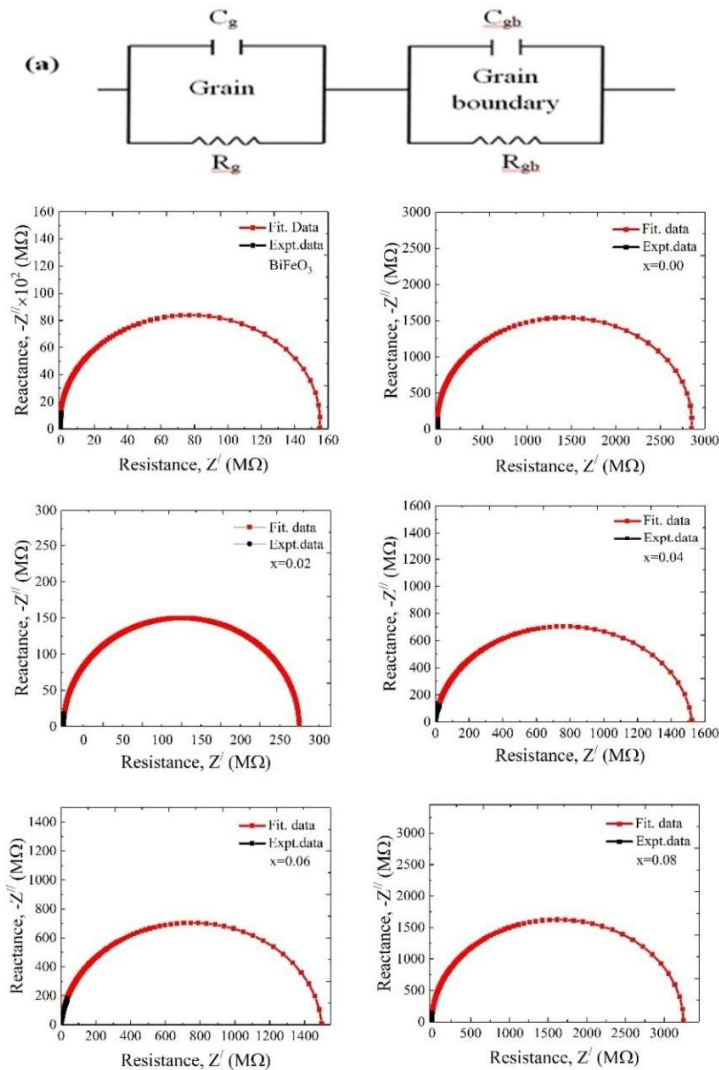


Figure 5: Cole–Cole plot of $\text{Bi}_{0.95}\text{Gd}_{0.05}\text{Fe}_{1-x}\text{Cr}_x\text{O}_3$ ceramic.

The Maxwell-Wagner double-layer model helps explaining the increase in AC conductivity in the high frequency region. In this model, the dielectric structure was supposed to be made up of two layers. The first layer is made up of a relatively good conductors separated by the second thin layers (grain boundaries) made up of comparatively poor conductors. Conductivity differences and high resistances between grain boundaries increase the dielectric constant, which is proportional to polarization and accretion of charge carrier in separated boundaries. Because, the electron exchange can't keep up with the external alternating electric field's growing frequency, polarization decreases and reaches a constant value at high frequencies. As a result, the relaxation time of grain boundaries is longer than that of conducting grains. So, conductivity is affected by both grains and grain boundaries (Matin, 2019). The rise in AC is due to grains playing a more active role at high frequencies, which promotes higher charge transfer in surrounding grains and, as a result, increased conductivity (Matin and Hossain *et al.*, 2019). A substantial number of grain boundaries are active in the low frequency domain, resulting in the least conduction mechanism within the studied samples. The obtained ac conductivity follows Joncher's law: $\sigma_{AC}(\omega) = \sigma_0 + \Psi\omega^s$, where $\sigma_{AC}(\omega)$ is the electrical conductivity, σ_0 is the frequency independent dc conductivity, Ψ is the temperature dependent exponential factor (Matin, 2019, Rhaman, 2020). Consider the power-law

exponents depend on temperature from 0 to 1. Figure 4 (b) depicts the variation of $\log(\sigma_{AC})$ with $\log(\omega^2)$ is used to compute the power factor (s). The obtained s values for various compositions are in the range of 0 to 1, implying charge carrier hopping within the sites.

The complex impedance spectra are important for materials that acquire one or more relaxation processes separately with a comparable amplitude and which follows the Cole-Cole structural forms. The Cole-Cole plot of $\text{Bi}_{0.95}\text{Gd}_{0.05}\text{Fe}_{1-x}\text{Cr}_x\text{O}_3$ nanoscale particles is shown in Figure 5. A single semicircular form can be seen in the impedance spectrum. Fitted data is represented by red semi-circular arcs, while experimental data is represented by black lines. It indicates that the conductive and dielectric characteristics are very homogeneous. The single semicircular arc pattern varies with composition, indicating that the Z'/Z'' ratio adapts as the Cr dopant concentration increases.

Complex dielectric modulus has also been investigated. The dielectric modulus (M^*) formulation proposed by Macedo *et al.* (Matin, 2019) is as follows:

$$M^*(\omega) = \frac{1}{\epsilon^*} = \frac{1}{\epsilon' - j\epsilon''} = \frac{\epsilon'}{\epsilon'^2 + \epsilon''^2} + j \frac{\epsilon''}{\epsilon'^2 + \epsilon''^2} = M'(\omega) + jM''(\omega) \quad (1)$$

In equation (1) substituting ϵ'' by $\epsilon' \tan\delta$ one might get

$$M^*(\omega) = M'(\omega) + jM''(\omega) = \frac{1}{\epsilon'(1 + \tan^2\delta)} + \frac{\tan\delta}{\epsilon'(1 + \tan^2\delta)} \quad (2)$$

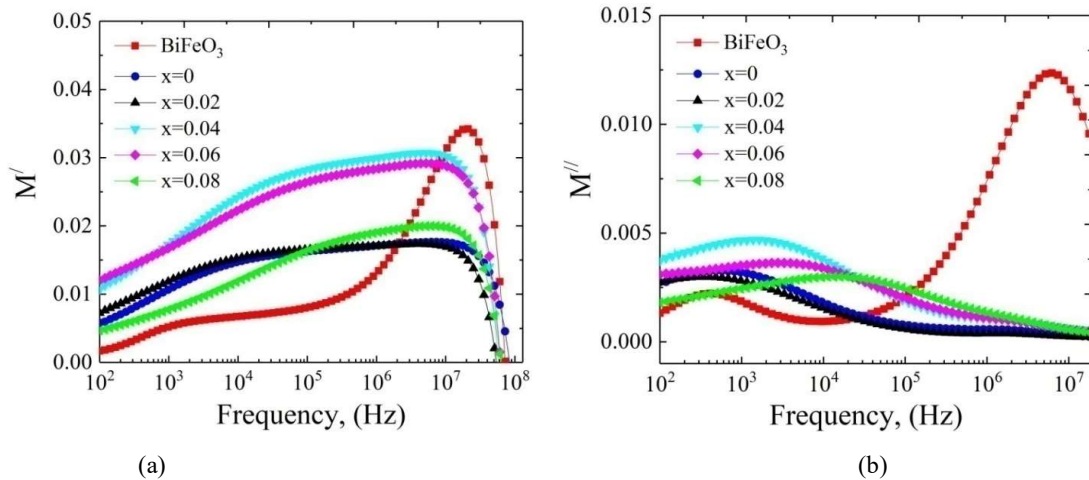


Figure 6: Complex electric modulus of $\text{Bi}_{0.95}\text{Gd}_{0.05}\text{Fe}_{1-x}\text{Cr}_x\text{O}_3$ ceramics: (a) Real part and (b) Imaginary part.

Figure 6(a) shows the real component (M') of the complex dielectric modulus as a function of frequency. M' is shown to grow with frequency up to 10^7Hz before sharply decreasing beyond that. Lower M' values in the low-frequency band indicate the presence of significant electronic and/or ionic polarization. The conduction process can be aided by dispersion for un-doped samples at higher frequencies. It could happen because charge carriers have a short range of motion. This denotes the charge flow's restorative force trailing under the influence of an external electric field (Matin, 2019).

The imaginary component (M'') of the complex dielectric modulus varies with frequency, as shown in Figure 6(b). The range in which charge carriers can travel long distances is defined by the region below the peak frequency. The charge carrier moves at short distances beyond the peak frequency (Ali, 2019; Pattanayak, 2014). The peak's location indicates a shift from long-distance to short-distance mobility. Asymmetrical peak broadening can be seen at both ends of the maxima. The presence of asymmetric peak broadening suggests that relaxation times are distributed over different time constants (Pattanayak, 2013; Ali, 2017). The relaxation peaks for the un-doped sample are at $0.5 \times 10^3\text{ Hz}$ and 10 MHz . The relaxation peak is noted to be shifted to the higher frequency owing to the Gd-Cr co-doping. At the high-frequency range, M'' decreases insignificantly for all doped samples that may be attributed to the limitation of charge carriers in potential wells refers the higher loss of ferroelectric properties.

4. CONCLUSIONS

$\text{Bi}_{0.95}\text{Gd}_{0.05}\text{Fe}_{1-x}\text{Cr}_x\text{O}_3$ ($x = 0, 0.02, 0.04, 0.06, \text{ and } 0.08$) were successfully synthesized by sol-gel method. The average crystallite size ranges in between 25 to 68 nm. Gd doping leads a sudden decrease of dielectric constant while it is further increases owing to the Cr doping. For a wide range of frequencies, the dielectric permittivity of doped BFO has been proven to be invariant. In Gd-Cr co-doped samples, the ac conductivity is dramatically lowered and the conductivity is resulted in due to the charge carrier hopping within the sites. In the cole-cole plot,

all doped samples showed a characteristic partial semicircular arc implying the predominant role of grain boundary resistance. Existence of dielectric relaxation behavior is confirmed where the relaxation decreases due to both Gd-Cr co-doping balance between two interstitial sites to effective locked maximum number of charge carriers conduction. The consequent effects of Cr doping significantly increase the dielectric characteristics of Gd-doped BFO and the improved dielectric permittivity implies that it could be used in both high and low-frequency devices.

REFERENCES

- Ali M. A., Khan M. N. I., F.-U.-Z. Chowdhury, Hossain M. M., Akhter Hossain A. K. M., Nahar A., Hoque S. M., Matin M. A., Uddin M. M.; 2019. Yttrium substituted Mg-Zn ferrites: correlation of physical properties with Yttrium content, *Journal of Materials Science: Materials in Electronics* 30, 13258–13270. <https://doi.org/10.1007/s10854-019-01689-z>
- Ali M. A., Uddin M. M., Khan M. N. I., F.-U.-Z. Chowdhury, Hoque S. M. 2017. Structural, morphological and electrical properties of Sn-substituted Ni-Zn ferrites synthesized by double sintering technique, *Journal of Magnetism and Magnetic Materials*, 424, 148-154. <https://doi.org/10.1016/j.jmmm.2016.10.027>
- Allibe J., Fusil S., Bouzouane K., Daumont C., Sando D., Deranlot E. J. C, Bibe M., and Barthelemy A., 2012. Room temperature electrical manipulation of giant magnetoresistance in spin valves exchange-biased with BiFeO₃, *Nano Lett.*, 12:1141. <https://doi.org/10.1021/nl202537y>
- Baettig P., Spaldin N. A. 2005. Ab initio prediction of a multiferroic with large polarization and magnetization, *Appl. Phys. Lett.* 86, 012505. <https://doi.org/10.1063/1.1843290>
- Bielecki J., Svedlindh P., Tibebu D. T., Cai S., Eriksson S. G. and Borjesson L. 2012. Structural and magnetic properties of isovalently substituted multiferroic BiFeO₃: insights from Raman spectroscopy, *Phys Rev B*, 86:184422, 2012. <https://doi.org/10.1103/PhysRevB.86.184422>
- Catalan, G., Scott J. F., 2009. Physics and applications of bismuth ferrite, *Adv. Mater.* 21, 2463–2485; DOI:10.1002/ADMA.200802849
- Chaudhuri A. and Mandal K., 2012. Enhancement of ferromagnetic and dielectric properties of lanthanum doped bismuth ferrite nanostructures, *Mater Research Bull.*, 47: 105761. <https://doi.org/10.1016/j.materresbull.2011.12.034>
- Chauhan S., Kumar M., Chhoker S., Katyal S. C., Jewariya M., and Suma B. N., 2015. Structural modification and enhanced magnetic properties with two phonon modes in Ca-Co co-doped BiFeO₃ nanoparticles, *Ceram Int*, 41:1430614. DOI:10.1016/j.ceramint.2015.07.062
- Chauhan S., Arora M., Sati P. C., Chhoker S., Katyal S. C. and Kumar M., 2013. Structural, vibrational, optical, magnetic and dielectric properties of Bi_{1-x}Ba_xFeO₃ nanoparticles, *Ceram Int*, 39:6399405. DOI:10.1016/J.CERAMINT.2013.01.066
- Dong S., Liu J -M., Cheong S -W., Ren Z. 2015. Multiferroic materials and magnetoelectric physics: symmetry, entanglement, excitation, and topology, *Adv. Phys.* 64, 519–626, doi:10.1080/00018732.2015.1114338.
- Dutta D. P., Tyagi A. 2018: Effect of Sm³⁺ and Zr⁴⁺ co-doping on the magnetic, ferroelectric and magnetodielectric properties of sonochemically synthesized BiFeO₃ nanorods, *Appl. Surf. Sci.* 450, 429–440; <https://en.x-mol.com/paper/article/642851>
- Eerenstein W., Mathur N., Scott J. F., 2006: Multiferroic and magnetoelectric materials, *Nature*, 442, 759–765. <http://dx.doi.org/10.1038/nature05023>
- Jonscher A. K. 1977. The ‘universal’ dielectric response, *Nature* 267, 673. <https://doi.org/10.1038/267673a0>
- Khomskii D., 2009: Classifying multiferroics: Mechanisms and effects, *Physics*, 2:20. DOI: 10.1103/Physics.2.20
- Khomchenko V. A., Karpinsky D. V., Paixão J. A., 2017. Magnetostructural correlations in BiFeO₃-based multiferroics, *J. Mater. Chem. C*, 5, 3623–3629. DOI: 10.1039/C9TC01521C
- Kumar A, Yadav K. L. 2011. Magnetic, magnetocapacitance and dielectric properties of Cr doped bismuth ferrite nano ceramics, *Materials Science and Engineering B* 176, 227– 230. DOI:10.1016/j.mseb.2010.11.012
- Kumar P. and Kar M., 2014. Effect of structural transition on magnetic and optical properties of Ca and Ti dual-doped BiFeO₃ ceramics, *Journal of Alloys and Compounds*, 584:566. DOI:10.1016/j.jallcom.2013.09.107
- Kuo C-Y., Hu Z., Yang J. C., Liao S-C, Huang Y. L., Vasudevan R. K., Okatan M. B. 2016. Single-domain multiferroic BiFeO₃ films, *Nature communications* 7, no. 1: 1-7; doi: 10.1038/ncomms12712
- Matin M. A., Rhaman M. M., Hossain M. N., Mozahid F. A., Hakim M. A., Rizvi M. H. and Islam M. H. 2019. Effect of preparation routes on the crystal purity and properties of BiFeO₃ nanoparticles, *Transactions on Electrical and Electronic Materials (Springer)*, Vol. 20, pp. 485 – 493. <https://doi.org/10.1007/s42341-019-00140-8>

- Matin M. A., Hossain M. N., Ali M. A., Hakim M. A., Islam M. F., 2019. Enhanced dielectric properties of prospective $\text{Bi}_{0.85}\text{Gd}_{0.15}\text{Fe}_{1-x}\text{Cr}_x\text{O}_3$ multiferroics, *Results in Physics*, ELSEVIER, Volume 12, Pages 1653-1659, ISSN 2211-3797. <https://doi.org/10.1016/j.rinp.2019.01.079>
- Matin M. A., Hossain M. N., Hakim M. A., and Islam M. F. 2019. Effects of Gd and Cr co-doping on structural and magnetic properties of BiFeO_3 nanoparticles, *Materials Research Express* 6, no. 5: 055038. <https://orcid.org/0000-0001-6905-4232>
- Matin M. A., Hossain M. N., Rhaman M. M. 2019. Dielectric and optical properties of Ni-doped LaFeO_3 nanoparticles, *SN Appl. Sci.* 1, 1479. <https://doi.org/10.1007/s42452-019-1453-9>.
- Mukherjee A., Basu S., Manna P. K., Yusuf S. M., Pal M., 2014. Giant magnetodielectric and enhanced multiferroic properties of Sm doped bismuth ferrite nanoparticles, *J. Mater. Chem. C*, 2, 5885–5891. <https://doi.org/10.1039/C4TC00591K>
- Mao W., Li X., Li Y., Li P., Bao G., and Yang T. 2012. Structural and magnetic properties of single-phase $\text{Bi}_{0.9}\text{Eu}_{0.1}\text{Fe}_{0.95}\text{Co}_{0.05}\text{O}_3$ and $\text{Bi}_{0.9}\text{Eu}_{0.05}\text{La}_{0.05}\text{Fe}_{0.95}\text{Co}_{0.05}\text{O}_3$ nanoparticles, *Mater Lett*, 76:1357. DOI:10.1016/j.matlet.2012.02.082
- Pattanayak S., Parida B. N., Das P. R. 2013. Impedance spectroscopy of Gd-doped BiFeO_3 multiferroics, *Appl. Phys. A* 112, 387–395. <https://doi.org/10.1007/s00339-012-7412-6>
- Pattanayak S., Choudhary R. N. P., Das P. R., Shannigrahi S. R. 2014. Effect of Dy-substitution on structural, electrical and magnetic properties of multiferroic BiFeO_3 ceramics, *Ceramics International*, Volume 40, Issue 6, Pages 7983-7991, ISSN 0272-8842, <https://doi.org/10.1016/j.ceramint.2013.12.148>.
- Qi, X. W., Zhang X. Y., Qi J. Q., Xu H. J., and Wang H. F., 2012. Preparation and dielectric properties of Cr doped multiferroic BiFeO_3 , *Key Engineering Materials*, vol. 512, pp. 1240-1243. Trans Tech Publications Ltd. <https://doi.org/10.4028/www.scientific.net/KEM.512-515.1240>
- Rhaman M. M., Matin M. A., Hossain M. N., Mozahid F. A., Hakim M. A., Islam M. F. 2019. Bandgap engineering of cobalt-doped bismuth ferrite nanoparticles for photovoltaic applications, *Bull. Mater. Sci.* 42:190, springer, <https://doi.org/10.1007/s12034-019-1871-8>.
- Rhaman M. M., Matin MD. A., Hossain M. N., Md. Nazrul Islam Khan,–Hakim M. A., Islam M. F. 2020. Ferromagnetic, electric, and ferroelectric properties of samarium and cobalt co-doped bismuth ferrite nanoparticles, *Journal of Physics and Chemistry of Solids*, 147,-109607, <https://doi.org/10.1016/j.jpics.2020.109607>
- Sosnowskat I., Peterlin-Neumaier T. and E. Steichele E. 1982. Spiral magnetic ordering in bismuth ferrite, *J. Phys. C: Solid State Phys.*, 15:4835. <http://iopscience.iop.org/0022-3719/15/23/020>
- Si Y. H., Xia Y., Shang S.-K., Xiong X.-B., Zeng X. R. Zhou J., Li Y.-Y. 2018. Enhanced Visible Light Driven Photocatalytic Behavior of BiFeO_3 /Reduced Graphene Oxide Composites, *Nanomaterials* 8, 526. doi: 10.3390/nano8070526
- Wang J. Li M., Liu X., Liu W., Hu Z., and Wang S. 2013. Improvements of the dielectric permittivity and ferromagnetic property of Co doped BiFeO_3 nanotubes, *J Porous Mater*, 20:72731. <https://doi.org/10.1007/s10934-012-9647-1>
- Wohlfeld K., Daghofer M., Oleś A. M. 2011. Spin-orbital physics for p orbitals in alkali RO₂ hyperoxides- Generalization of the Goodenough-Kanamori rules, *EPL (Europhysics Lett.* 96, 27001. doi:10.1209/0295-5075/96/27001
- Wu J., Fan Z., Xiao D., Zhu J., and Wang J., 2016. Multiferroic bismuth ferrite-based materials for multifunctional applications: Ceramic bulks, thin films and nanostructures, *Prog. Mater. Sci.*, 84:335–402. DOI: 10.1016/J.PMATSCI.2016.09.001
- Yoo Y. J., Hwang J. S., Lee Y. P., Park J. S.,–Rhee J. Y., Kang J.-H., Lee K. W., Lee B. W., Seo M. S. 2015. Origin of enhanced multiferroic properties in Dy and Co co-doped BiFeO_3 ceramics, *J. Magn. Magn. Mater.* 374, 669–675. doi:10.1016/J.JMMM.2014.09.034.
- Yu L., Deng H., Zhou W., Zhang Q., Yang P., Chu J. 2016. Effects of (Sm, Mn and Ni) co-doping on structural, optical and magnetic properties of BiFeO_3 thin films fabricated by a sol-gel technique, *Mater. Lett.* -170, 85–88. 10.1016/j.matlet.2016.02.004
- Zheng T., Zhao C., Wu J, Wang, K. and Li L. F., 2018. Large strain of lead-free bismuth ferrite ternary ceramics at elevated temperature, *Scripta Mater*, 155:11–15. DOI:10.1016/J.SCRIPTAMAT.2018.06.007.